

The X-Ray Telescope onboard Suzaku

Peter J. SERLEMITOS, Yang SOONG, Kai -Wing CHAN, Takashi OKAJIMA, John P. LEHAN
NASA, Goddard Space Flight Center, Code 662, Greenbelt, MD20771, USA

Yoshitomo MAEDA, Kei ITOH, Hideyuki MORI, Ryo IIZUKA, Akiharu ITOH,
Hirohiko INOUE, Shunsaku OKADA, Yushi YOKOYAMA, Yumi ITOH, Masatoshi EBARA,
Ryoko NAKAMURA, Kensuke SUZUKI
Institute of Space and Astronautical Science, JAXA
3-1-1 Yoshinodai, Sagamihara, Kanagawa 229-8510

Manabu ISHIDA, Akira HAYAKAWA, Chiaki INOUE, Satoshi OKUMA, Ren KUBOTA,
Masaki SUZUKI, Takeyuki OSAWA
Department of Physics, Tokyo Metropolitan University,
1-1 Minami-Osawa, Hachioji, Tokyo 192-0397
ishida@phys.metro-u.ac.jp

Koujun YAMASHITA, Hideyo KUNIEDA, Yuzuru TAWARA, Yasushi OGASAKA,
Akihiro FURUZAWA, Keisuke TAMURA, Ryo SHIBATA, Yoshito HABA, Masataka NAITOU
Department of Particle and Astrophysics, Nagoya University,
Furo-cho, Chikusa-ku, Nagoya 464-8602

and

Kazutami MISAKI
Max-Planck-Institut fuer extraterrestrische Physik, D-85741, Garching, Germany

(Received 2006 June 30; accepted 2006 July 1)

Abstract

We present the design parameters, production process, and in-flight performance of the X-ray telescopes (XRTs) onboard Suzaku. The imaging capability is significantly improved over the ASCA XRT, which had half-power diameters of $3'6''$, to $1'8''$ – $2'3''$ for all four XRT-I modules. The optical axes are found to be distributed within a radius of $1'3''$, which makes the observation efficiency of all the XRTs more than 97% at the XIS-default observing position. The vignetting over the XIS field of view predicted via ray-tracing coincides with that measured for observations of the Crab Nebula to within $\sim 10\%$. Contemporaneous fits of a power law to all the XIS spectra of the Crab Nebula taken at the two standard observing positions (XIS/HXD-default positions) gives a flux consistent with that obtained by Toor & Seward (1974) to within $\sim 2\%$. The pre-collimator on the top of each XRT module successfully re-

duces the intensity of the stray light from the 20' and 50'-off directions down to the level of pre-flight expectations.

Key words: Instruments: detectors — Telescopes — X-rays: general

1. Introduction

The X-ray telescope onboard the Einstein observatory (Van Speybroeck 1979) represented dramatic improvements in both spatial resolution and sensitivity, and thereby allowed for great advances in X-ray astronomy both qualitatively and quantitatively. Since this time, X-ray telescopes have gradually become essential to X-ray astronomy, and were adopted for both EXOSAT (de Korte et al. 1981) and ROSAT (Aschenbach 1988).

Another breakthrough was made by the thin-foil-nested X-ray telescopes onboard BBXRT (Serlemitsos 1988) and ASCA (Serlemitsos et al. 1995). These mirrors allowed for the first time the ability to reflect X-rays up to ~ 10 keV. This unprecedented capability enables the investigation of the astrophysically important iron K-shell features, which have been observed from various classes of celestial objects, both in detail and for much fainter sources. Further, this technology, along with the energy-resolving power of the CCDs (Burke et al. 1991), has helped to unveil the nature of thermal plasmas and of X-ray-irradiated nebulae. In order to efficiently reflect high energy X-rays, the incident grazing angle θ of the reflector must be within $\lesssim 0.7^\circ$. In such ultimate grazing-incidence geometries, the area effective for photon collection becomes only a tiny fraction ($\sim \sin \theta$) of the geometric area of the reflectors. To overcome this disadvantage, a number of reflectors are tightly nested confocally and coaxially. In addition, it is important to make the reflector substrate as thin as possible for high aperture efficiency, because the substrate edge forms a dead area. The idea of a thin-foil-nested telescope has been successfully implemented for the X-ray telescopes onboard Beppo-SAX (Conti et al. 1994), XMM-Newton (Aschenbach 2002; Lumb et al. 2003), and Swift (Burrows et al. 2005).

The X-ray telescope onboard Suzaku (Mitsuda et al. 2006), hereafter referred to as XRT, is also a thin-foil-nested Wolter-I type telescope. Another type of X-ray telescope is one that achieves the ultimate imaging capability with accurate Wolter-I optics, which is onboard the Chandra X-ray Observatory (Weisskopf et al. 2002). Given a severe weight limit imposed by the launch vehicle for Suzaku, however, we have intended to achieve the maximum possible effective area particularly at the energy of the iron K lines. At the same time, the shapes of the primary and secondary reflectors, a paraboloid and hyperboloid, respectively, in the original Wolter type I optics, are both approximated by cones in Suzaku, since they are very similar in their grazing optics. This approximation ultimately limits the imaging capability of the Suzaku XRT, in that the image in the focal plane cannot be smaller than $\ell \tan \theta$ in principle, where ℓ and θ are the axial length and the grazing angle of a typical reflector (Kunieda et al. 2001). In

the case of the Suzaku XRT, this results in the Half-Power Diameter (HPD) of $\sim 18''$.

Since ASCA, improvement have been made in three areas. First, the incident grazing angle has been reduced to be $\lesssim 0.6^\circ$ so that even the outermost mirror shell can reflect the iron K photons. The diameter of the X-ray telescope has increased from ~ 350 mm to ~ 400 mm. Accordingly, the focal lengths are extended to 4.50 m and 4.75 m, compared with that of 3.5 m for ASCA. Second, the smoothness of the ASCA reflectors was achieved by coating the acrylic lacquer on the rolled aluminum substrate followed by vacuum deposition of a gold layer on top of it. However, there remains a mid frequency figure error on the surface of the lacquer, which results in image broadening. We therefore have adopted the replica method for producing the Suzaku reflectors (Serlemitsos & Soong 1996). In this method, the gold layer is sputtered onto a glass tube of highly smooth surface and is transferred to a reflector substrate with epoxy as adhesive. This improves the HPD from $\sim 3.6'$ for ASCA to $\sim 1.9'$ for Suzaku. Finally, since the reflectors are tightly packed in the mirror housing, X-rays arriving from outside the field of view can be reflected by adjacent surfaces or skip the normal reflections and then appear as X-ray images in the field of view. In order to avoid such stray light, we have provided a pre-collimator on top of each XRT (Mori et al. 2005). We install five XRT modules on the top plate of the Extensible Optical Bench (EOB). One is referred to as the XRT-S which has a focal length of 4.50 m and was adapted to the X-Ray Spectrometer (XRS; X-ray micro-calorimeter; Kelley et al. (2006)). The other four modules are designated as XRT-I0, I1, I2, I3 with a focal length of 4.75 m, and are dedicated for the X-ray Imaging Spectrometer (XIS; X-ray CCD camera; Koyama et al. (2006)). Since Suzaku is the revival mission of Astro-E1, which failed to reach orbit on 2000 February 10 (Inoue 2003), the basic design and performance verified in the ground-based calibration have already been published (Kunieda et al. 2001; Shibata et al. 2001; Misaki et al. 2005).

In this paper, we present first the design parameters of the Suzaku XRT in section 2. The expected performance on the basis of the ground-based calibration is also described. In section 3, characteristics of the Suzaku XRTs such as effective area, imaging capability, and vignetting, are summarized based on in-flight data. A summary is provided in section 4.

2. Design Parameters and Expected Performance from Ground Measurements

2.1. Telescope Design

The design parameters of the X-ray telescope onboard Astro-E1 launched on 2000 February 10 are described in full detail in Kunieda et al. (2001). The basic telescope design of Suzaku has not been changed since Astro-E1, except for the pre-collimator newly adopted for Suzaku. The reader is referred to this paper for more details on the Suzaku XRT.

In table 1, we summarize all the design parameters of the Suzaku XRT. The primary constraint on the size of the XRT originates from the maximum possible focal length, which

Table 1. X-Ray Telescope Design Parameters

	XRT-I	XRT-S	ASCA
Focal Length	4.75 m	4.50 m	3.50 m
Number of Module	4	1	4
Substrate			
Material	Aluminum	Aluminum	Aluminum
Substrate Thickness	152 μm	152 μm	127 μm
Axial Length	101.6 mm	101.6 mm	101.6 mm
Reflector			
Material	Au	Au	Au
Thickness	$> 1000 \text{ \AA}$	$> 1000 \text{ \AA}$	500 \AA
Adhesive material	Epoxy	Epoxy	Acrylic lacquer
Adhesive thickness	25 μm	25 μm	10 μm
Number of Nesting	175	168	120
Diameter of innermost reflector	118 mm	119 mm	120 mm
Diameter of outermost reflector	399 mm	400 mm	345 mm
Incident angle	$0^\circ 18\text{--}0^\circ 60$	$0^\circ 19\text{--}0^\circ 63$	$0^\circ 24\text{--}0^\circ 70$
Number of Reflectors/Telescope	1400	1344	960
Geometrical Area/Telescope	873 cm^2	887 cm^2	558 cm^2
Weight/Telescope	19.3 kg	19.9 kg	9.84 kg
Field of View ^a			
at 1 keV	20'	20'	24'
at 7 keV	14'	14'	16'
Effective Area (per XRT) ^b			
at 1.5keV	450 cm^2	450 cm^2	300 cm^2
at 7.0keV	250 cm^2	250 cm^2	150 cm^2
Spatial Resolution (HPD) ^b	2'0	2'0	3'6

^a Diameter of the area within which the effective area is more than 50% of the on-axis value.

^b Measured on the ground.

is 4.75 m for XRT-I, determined by the space within the nose fairing of the M-V rocket. For XRT-S, the XRS detector array is within a dewar, located ~ 70 cm above the base plate of the spacecraft. Accordingly, we inserted the mirror support with a length of 59 cm between the top plate of EOB and XRT-S, and achieved a focal length of 4.50 m. In Fig. 1 we give a schematic view of the XRTs mounted on the top plate of the EOB. Given the focal length, the diameter of the telescope is determined by the requirement that the iron K-shell emission lines (< 7 keV) should be efficiently reflected even by the outermost reflector shell. This results in an outermost radius of $r_{out} = 200$ mm, where the incident grazing angle of $0^\circ 60$ and $0^\circ 63$ for

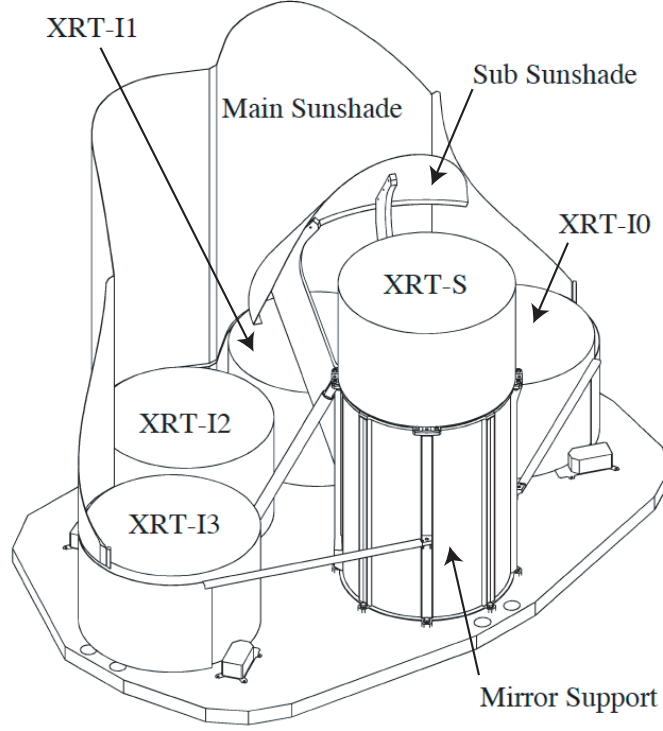


Fig. 1. Schematic view of the Suzaku XRTs mounted on the top plate of the Extensible Optical Bench (EOB). By courtesy of K. Abe, NIPPI Corporation.

the XRT-I and XRT-S, respectively. Note that $0^{\circ}60$ corresponds to the critical grazing angle of gold for the total reflection of the 7.65 keV X-ray. Within the radius of 200 mm, the reflector shells are confocally nested with the ultimate tightness where X-rays from the on-axis direction be reflected by the primary reflectors, whereas the entire surface of any primary reflector is never shaded by the inner adjacent primary reflector. This determines the total number of nestings, 175 and 168, for the XRT-I and the XRT-S, respectively. Fig. 2 gives a picture of one of the telescope modules, XRT-I1.

Finally, the number of XRT-I modules is determined to be four, by taking into account the available area of the EOB top plate. Fig. 3 gives the total effective area of the four XRT-I modules, including the detector efficiency, in comparison with that of XMM-Newton (PN + 2MOS) and Chandra (ACIS-I and ACIS-S). The effective areas for Chandra were calculated from the ARF files prepared for proposal planning of the AO2 cycle¹, while those for XMM were from the ARF prepared for the nominal position using CALINDEX #0122². Although the total weight is only $\lesssim 80$ kg, the effective area of the four XRT-I modules at 7 keV is comparable to that of XMM-Newton mirrors whose total weight is as much as 1311 kg.

¹ <http://asc.harvard.edu/>

² <http://xmm.vilspa.esa.es/>

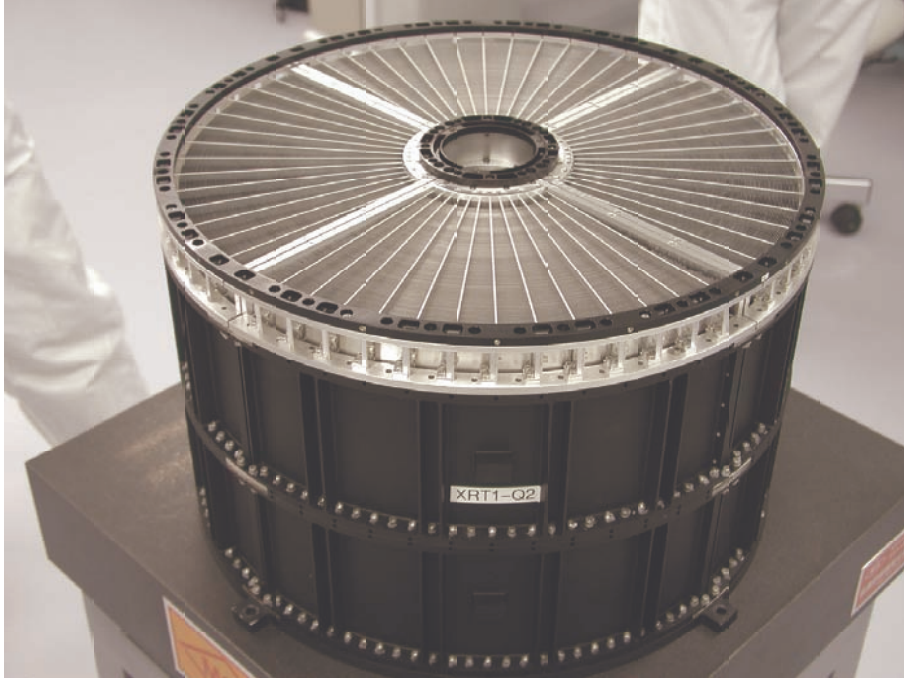


Fig. 2. Picture of the module XRT-I1. Note that the thermal shield is not yet attached.

2.2. Reflectors

The reflectors of the Suzaku XRT were produced through a replication method (Serlemitsos & Soong 1996) in which a thin ($\gtrsim 1000\text{\AA}$) gold layer sputtered on a highly smooth glass tube is transferred to an aluminum substrate with epoxy as adhesive. We adopted #2024 aluminum sheet with thickness of $152\text{ }\mu\text{m}$ ($= 6.0\text{ mil}$) as the substrate of the reflector for its stiffness and lightness. It is first cut into fan shape, which is deployed as a quarter of a cone, and then formed into conical shape in an oven at 200°C for 8 hr, by being pushed onto a shaping mandrel with air pressure. The shaping mandrels are mechanically polished as smoothly as $2\text{--}3\text{ }\mu\text{m}$ in peak-to-bottom. This process finally determines the shape of each reflector. In the meantime, gold is sputtered in a vacuum chamber onto a cylindrical glass mandrel which is a borosilicate glass tube produced by Schott Glaswerke (Germany). Gold is used as an agent to separate the reflector from the glass mandrel as well as reflecting surface. The smoothness of the surface of the glass tube is equivalent to that of float glass, with a micro roughness of only a few \AA . After these two processes, we spray epoxy as glue onto the inner side of the substrate until its thickness becomes $25\text{ }\mu\text{m}$. The epoxy of this amount is thick enough to fill a large-scale figure error of the substrate and to make the reflecting surface as smooth as that of the glass mandrel. The epoxy-sprayed substrate is adhered to the gold-layered glass mandrel in a vacuum chamber, and the epoxy is cured at 40°C for 8 hr. Finally, the substrate can easily be separated off at the boundary of the glass and the gold.

We have measured the surface shape of the reflector thus produced with optical laser

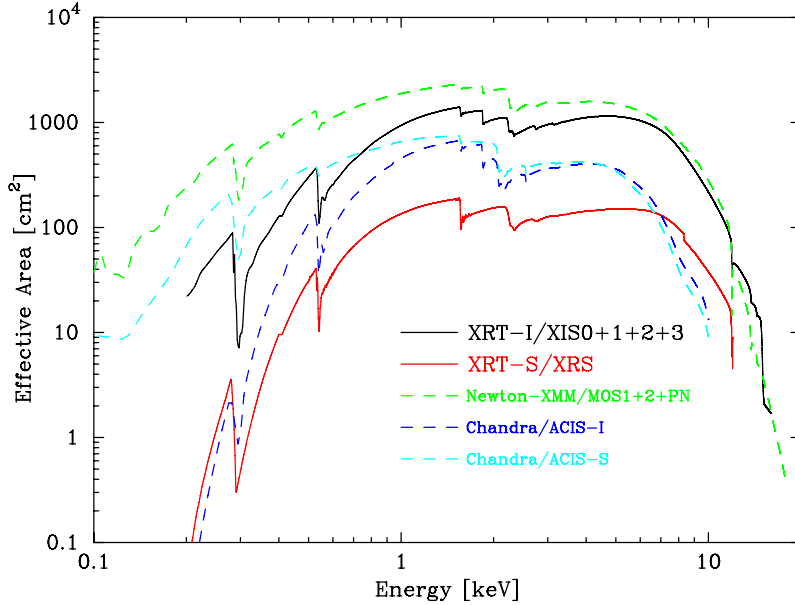


Fig. 3. Total effective area of the four XRT-I modules in comparison with that of XMM-Newton and Chandra. Transmissions of the thermal shield and the optical blocking filter, and the quantum efficiency of the CCD are all taken into account.

profilometers and by utilizing X-ray scattering. It is found that the amplitude of micro roughness with a surface wavelength of $\lesssim 30\mu\text{m}$ is as small as that of the Chandra reflector (Zissa 1999), whereas that with a surface wavelength of $\gtrsim 100\mu\text{m}$ is larger by several orders of magnitude (Misaki et al. 2005). In Fig. 4, we show the encircled-energy fraction (EEF) of one of the typical Suzaku quadrants at three different energies measured at the ISAS 30 m beam line (Shibata et al. 2001), in comparison with that of ASCA. The diameter to define the 100% flux is taken to be $24'$ for the ASCA XRT and $17'.8$ (= the size of the CCD chip) for the Suzaku XRT-I. The HPD is significantly improved from ASCA ($\sim 3'.6$). This is owing to the fact that the mid-frequency figure error of the acrylic lacquer surface of the ASCA reflector is significantly reduced by the replication method. Nevertheless, the HPD of $1'.9$ is still far from the design value of $\sim 0'.3$. This is due to the longer wavelength figure error remaining on the replica surface and positioning error or the reflectors in the housing of the XRT (Misaki et al. 2005). On the other hand, the HPD at the three energies are nearly identical, being slightly smaller at the highest energy 9.44 keV. This is a remarkable contrast with that of ASCA (Fig. 10 of Serlemitsos et al. (1995)), where the EEF becomes significantly broader at higher energies. This demonstrates that the micro roughness of the gold surface is so small that it does not affect the image blur in the Suzaku XRT. This is a significant merit of the replication method.

2.3. Pre-Collimator

It is known that ASCA observations were sometimes hampered by X-rays arriving from sources out of the field of view, which we refer to as stray light. In order to reduce this stray

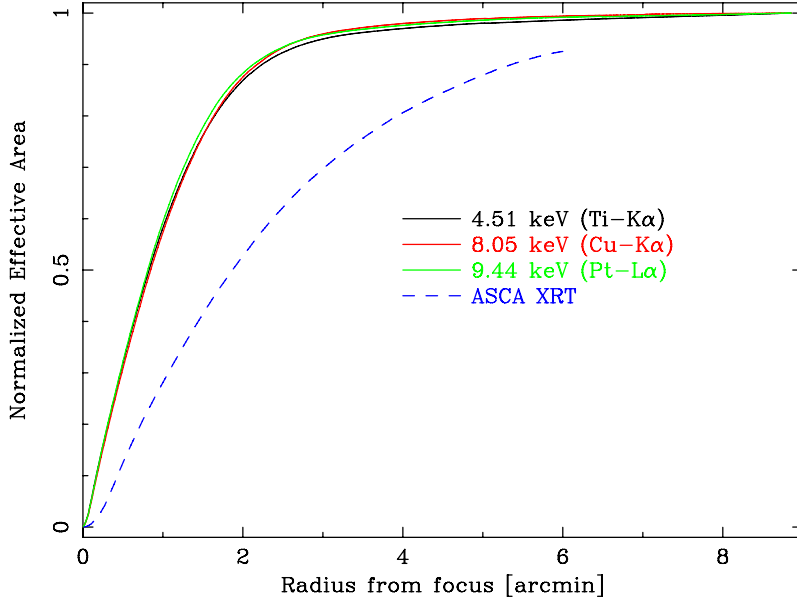


Fig. 4. Encircled-energy fraction (EEF) of a typical quadrant of XRT-I at the three energies 4.51 keV, 8.04keV, and 9.44keV, in comparison with that of ASCA measured at 4.51 keV. The diameter to define the 100% flux is $24'$ for the ASCA XRT and $17'8$ (= the size of the CCD chip) for the XRT-I quadrant.

light, we have planned to introduce a pre-collimator in front of the XRT for the first time. Its design, production process, and performance verification in the ground-based calibration are described in Mori et al. (2005) in full detail. Hence, we describe them only briefly here.

Since a number of reflectors are tightly installed in the telescope housing, it is possible that some X-rays are reflected/scattered in the housing on light paths other than the nominal double reflection. These abnormally reflected/scattered X-rays are potential candidates of stray light which form a ghost image within the detector field of view. Among various components of stray light, the “secondary reflection” and the “backside reflection” are the two major components whose paths are shown in Fig. 5. The “secondary reflection” is the light path where the incident X-ray is reflected only by the secondary reflector, whereas in the “backside reflection” the incident X-ray is first reflected by a backside of the primary reflector followed by undergoing the normal double reflection. For geometrical reason, these two components appear on the opposite side from the detector center, irrespective of the incident orientation of the stray light.

Since the “backside reflection” includes the reflection on a less shiny backside, the stray flux due to the “backside reflection” is at least a factor of 5–6 smaller than that of the “secondary reflection”. Hence, it is much more important to reduce the “secondary reflection”. For this to be achieved, it is easily understood from the Fig. 3 that the secondary reflection, arriving at the center of the field of view, in particular, can be cut if a cylindrical blade is placed just on top of the primary reflector. In order to suppress stray images from all “secondary reflections” within the XIS field of view, $17'8 \times 17'8$, a series of blades is needed whose height is

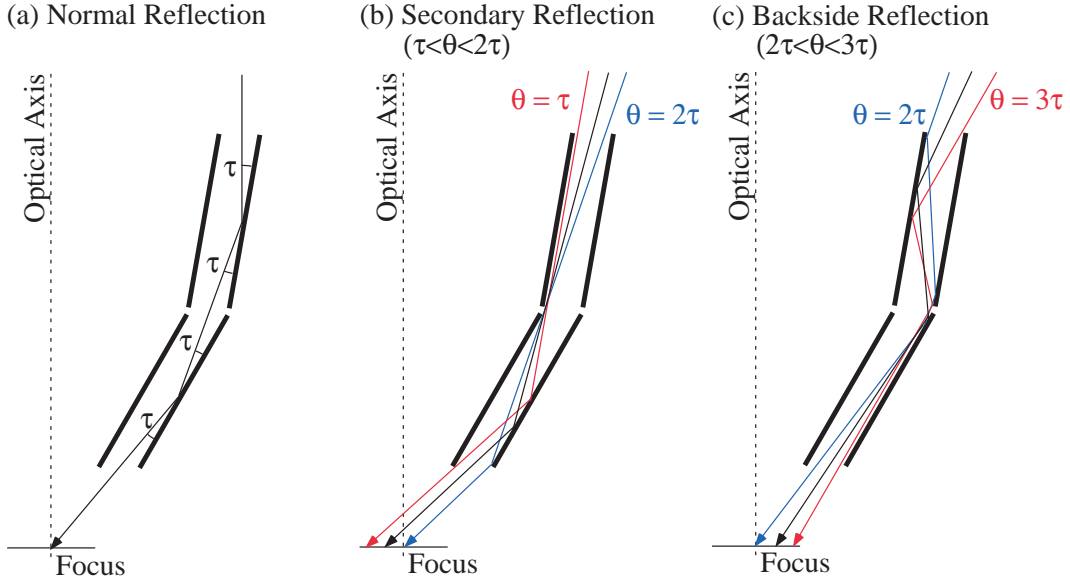


Fig. 5. Major reflection paths occurring in the XRT structure. τ represents the oblique angle of the primary reflector measured from the optical axis of the XRT: (a) Normal double reflection of the X-ray arriving from the on-axis direction. Incident X-rays are bent by the angle 4τ in total, and converge to the on-axis focus: (b) Secondary reflection, which arrives at the focal plane only if the incident angle of the X-ray θ measured from the optical axis is in the range $\tau < \theta < 2\tau$: (c) The stray light path that gives rise to the brightest ghost among various backside reflections, that is, the reflection at the backside of the primary followed by the normal double reflection. This pattern occurs when the X-ray incident angle is in the range $2\tau < \theta < 3\tau$. This figure is taken from Mori et al. (2005).

only 15 mm at the outermost radius but becomes gradually larger for inner shells (~ 76 mm at the innermost reflector shell). Since blades with this height cannot be compromised with the spacecraft design, we decided to unify the effective height of all the blades to be 30 mm. In table 2, we summarize the design parameters of the pre-collimator. The material of the blade

Table 2. Design parameters of the pre-collimator

	XRT-I	XRT-S
Blade		
Material	Aluminum	Aluminum
Thickness	120 μm	120 μm
Height	22 mm	22 mm
Effective height	30 mm	30 mm
Number of Nesting	175	168
Housing height	32 mm	32 mm
Weight/XRT	2.7 kg	2.7 kg

is again aluminum. In order for the blades to not stick out of the reflector width, they are

thinner than the reflector by roughly $\sim 50 \mu\text{m}$.

Because of the limited height of the blades, we cannot completely eliminate secondary reflections from off-axis angles in the range $11' - 30'$ (Fig. 5 of Mori et al. (2005)). In addition, although the top of the blades are located 30 mm above the primary reflectors, we need to have 8 mm space between the blade bottom and the reflector top. Unfortunately, X-rays arriving from off-axis angles of $60' - 70'$ pass through this space and form ghost images in the focal plane. However, the X-rays from off-axis directions in the range $20' - 70'$ are diminished by more than 90% compared to the case of no pre-collimator. This is of significant merit in observing the faint outer regions of diffuse sources such as clusters of galaxies, and reducing contamination due to the cosmic X-ray background. It is also important to note that the remaining ghost images due to secondary reflections concentrate on the edge of the field of view, and the detector center is nearly free from the secondary reflection, as demonstrated in Fig. 12 of Mori et al. (2005).

2.4. Thermal Shield

After the installation of the pre-collimator on top of each XRT, the entrance side is covered with a thermal shield, in order to isolate the XRT thermally from space as well as to reflect infrared radiation from the interior of the spacecraft. This is to keep the XRT temperature within the specified range of $20 \pm 7.5^\circ\text{C}$. The thermal shield also works to blocking optical light from the sky and from the surface of Earth illuminated by the sun.

In Fig. 6, we give a schematic view of the thermal shield. As for the XRT itself, the

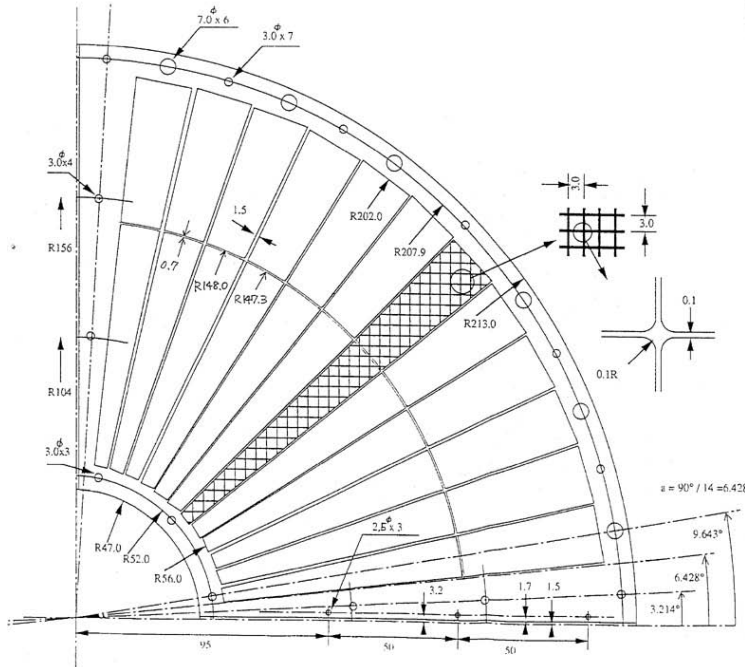


Fig. 6. Schematic view of the Suzaku thermal shield.

thermal shield is also produced as units of quadrants. The thermal shield is mechanically sustained by a frame made of aluminum, with a thickness of 4 mm. The frame has thirteen spokes which are along the alignment bars of the XRT. A stainless steel mesh with a wire pitch, width and thickness of 3 mm, 0.1 mm, and 0.15 mm, respectively, is glued with epoxy to the top side of the frame. Finally, a polyethylene terephthalate (PET) film as thin as $0.24\ \mu\text{m}$, coated with aluminum layer with thickness of 30 nm on the surface oriented to the space, is adhered to the mesh with epoxy.

Fig. 7 gives the transmission of X-rays as a function of energy. The data were taken at the

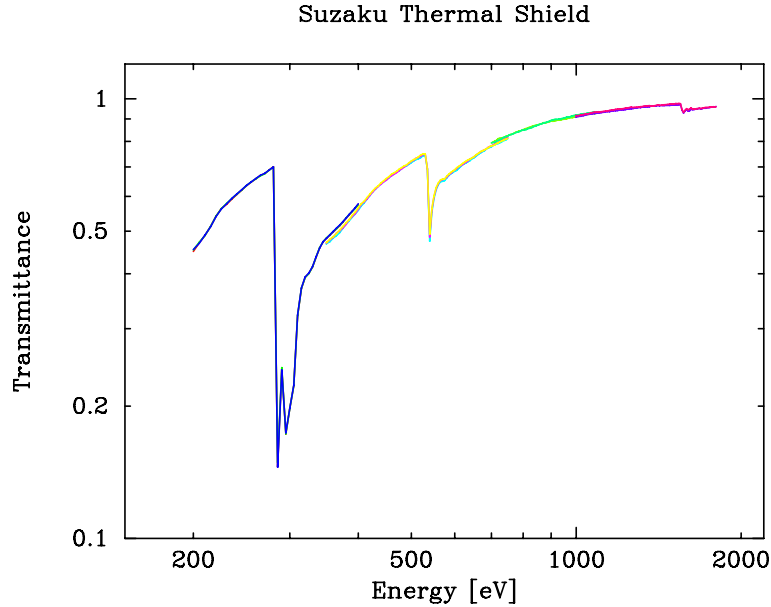


Fig. 7. Transmission of the thermal shield as a function of X-ray energy measured at the synchrotron beam facility SPring-8. Note that the transmission of the mesh is not included. Different colors indicate separate measurements carried out with a different grating apparatus.

beamline for soft X-ray spectroscopy (BL25SU) at the synchrotron radiation facility SPring-8. Note that the measurements are carried out only for the PET film with the aluminum coating. For the real thermal shield, the transmission of the stainless steel mesh 92.4 %, which is equal to the fraction of the geometrically open area, should additionally be multiplied. The K-shell absorption edges of carbon and oxygen can be identified at 0.28 keV and 0.53 keV, respectively. The wavy structure is due to XAFS associated with the K-edges. See Kunieda et al. (2001) for more detail about the thermal shield.

3. In-flight Performance

In this section we describe the in-flight performance and calibration of the Suzaku XRTs. Note that the XRS (Kelley et al. 2006) ran short of the coolant helium before observing celestial objects, and hence, there are no data to verify the in-flight performance of the XRT-S.

Accordingly, we hereafter concentrate on the four XRT-I modules (XRT-I0 through I3) which focus incident X-rays onto the XIS detectors.

3.1. Optical Axis

The maximum transmission of each telescope module is achieved when a target star is observed along the optical axis. The optical axes of the four XRT-I modules are, however, expected to scatter within an angular range of $\sim 1'$. Accordingly, we need to define the axis to be used for real observations that provides a reasonable compromise among the four optical axes. We hereafter refer to this axis as the observation axis.

In order to determine this observation axis, we have first searched for the optical axis of each XRT-I module by observing the Crab Nebula at various off-axis angles. The observations of the Crab Nebula were carried out in the following three groups. Hereafter all the off-axis angles are expressed in the detector coordinate system (Det-X, Det-Y) (Ishisaki et al. 2006).

1. 2005 Aug. 22 03:30UT – 15:33UT: a short observation near the center of the detectors, which is defined as the origin $(0', 0')$ of the (Det-X, Det-Y) scheme, until 06:00UT followed by the four $10'$ -off observations at $(\text{Det-X}, \text{Det-Y}) = (\pm 10', 0')$ and $(0', \pm 10')$.
2. 2005 Aug. 24 23:58UT – Aug. 27 07:30UT: a series of the off-axis observations at $(\text{Det-X}, \text{Det-Y}) = (\pm 3'.5, 0')$, $(0', \pm 3'.5)$, $(\pm 7'.0, 0')$, $(0', \pm 7'.0)$, $(\pm 20', 0')$, $(0', \pm 20')$, $(+50', 0')$ and $(+120', 0')$.
3. 2005 Sep. 15 01:00UT – Sep. 16 08:50UT: pointings at the XIS default position $(\text{Det-X}, \text{Det-Y}) = (0', 0')$ and the HXD default position $(\text{Det-X}, \text{Det-Y}) = (-3'.5, 0')$ as well as the remaining three $50'$ off pointings at $(\text{Det-X}, \text{Det-Y}) = (-50', 0')$ and $(0', \pm 50')$.

Note that the field of view of the XIS detector is a square with $17'.8$ on a side. Thus only the data taken at the origin, at $\pm 3'.5$ -off and at $\pm 7'.0$ -off are available for determining the optical axes.

By fitting a model of a Gaussian plus a constant to the count rate as a function of the off-axis angle, we determined the optical axis of each XRT-I module. The results are given in Fig. 8. Since the optical axes moderately scatter around the origin, we have decided to adopt it as the observation axis for XIS-oriented observations as the default. Hereafter we refer to this axis as the XIS-default orientation, or equivalently, the XIS-default position. The optical axis of XRT-I0 shows the largest deviation of $\sim 1'.3$ from the XIS-default position. Nevertheless, the efficiency of XRT-I0 at the XIS-default position is more than 97% even in the highest 8–10 keV band (see Fig. 11). The optical axis of the HXD PIN detector, on the other hand, deviates by $\sim 5'$ in the negative Det-X direction (Takahashi et al. 2006; Kokubun et al. 2006). Because of this, the observation efficiency of the HXD PIN at the XIS-default orientation is reduced to $\sim 93\%$ of the on-axis value. We thus provide another default pointing position, the HXD-default position, for HXD-oriented observations, at $(\text{Det-X}, \text{Det-Y}) = (-3'.5, 0')$. At the HXD-default position, the efficiency of the HXD PIN is nearly 100%, whereas that of the XIS is $\sim 88\%$ on

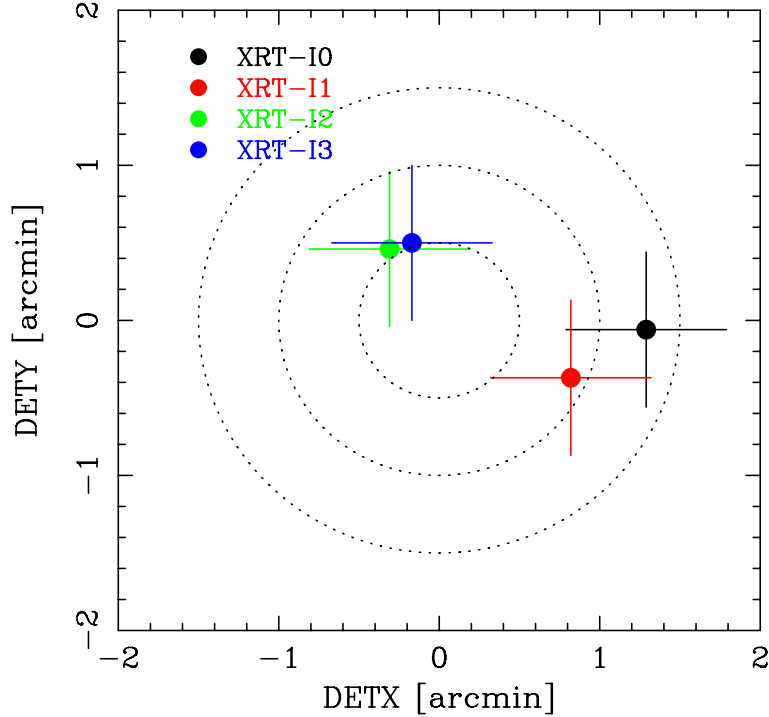


Fig. 8. Locations of the optical axis of each XRT-I module in the focal plane determined from the observations of the Crab Nebula in 2005 August–September. This figure implies that the image on each XIS detector becomes brightest when a target star is placed at the position of the corresponding cross. The dotted circles are drawn every $30''$ in radius from the XIS-default position (see the text).

the average.

3.2. Effective Area

In-flight calibration of the effective area has been carried out with the version 0.7 processed data (Mitsuda et al. 2006) of the Crab Nebula both at the XIS/HXD-default positions. The observations were carried out in 2005 September 15–16 (§3.1). The data were taken in the normal mode with the 0.1 s burst option in which the CCD is exposed during 0.1 s out of the full-frame read-out time of 8 s, in order to avoid event pile-up and telemetry saturation. The exposure time of 0.1 s is, however, comparable to the frame transfer time of 0.025 s. As a matter of fact, the Crab image is elongated in the frame-transfer direction due to so-called out-of-time events, as shown in Fig. 9. Accordingly, the background-integration regions with a size of 126 by 1024 pixels are taken at the left and right ends of the chip for the XIS-default position, perpendicularly to the frame-transfer direction, as shown in the left panel of Fig. 9. For observations at the HXD-default observation, the image center is shifted from the XIS-default position in the direction perpendicular to the frame-transfer direction for XIS0 and XIS3. Hence we can adopt the same background-integration regions as those of the XIS-default position for these two XIS modules. For XIS1 and XIS2, on the other hand, the image shift occurs in the frame-transfer direction, as shown in the right panel of Fig. 9. We thus take a

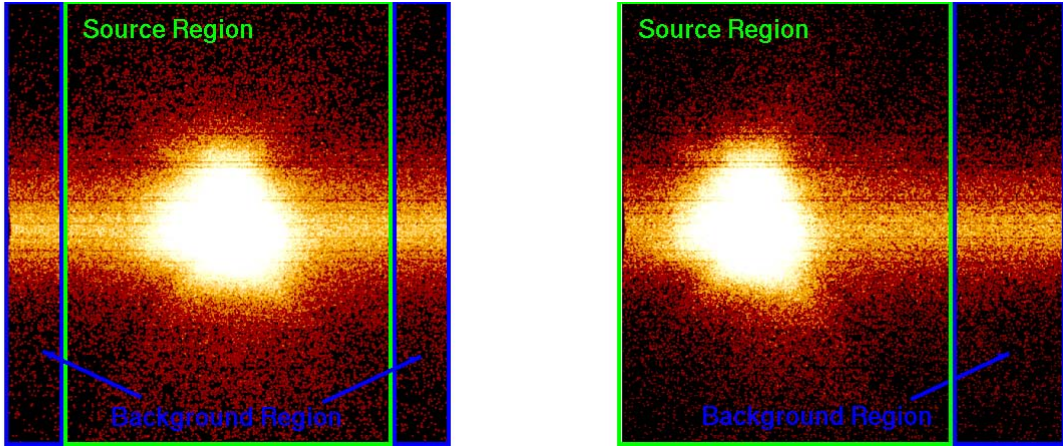


Fig. 9. The source- and background-integration regions overlaid on the Crab images taken with XIS1 at the XIS-default position (left) and the HXD-default position (right) on 2005 September 15-16. The images are elongated in the frame-transfer direction due to out-of-time events (see the text). In order to cancel these events, the background regions with a size of 126 by 1024 pixels each are taken at the left and right ends of the chip for the XIS-default position, and a single region with a size of 252 by 1024 pixels is taken at the side far from the Crab image for the HXD-default position. The remaining source-integration region has a size of 768 by 1024 pixels, or $13'3 \times 17'8$. The background subtraction is carried out after area-size correction.

single background-integration region with a size of 252 by 1024 pixels at the far side from the Crab image for the HXD-default position of these two detectors. As a result, the remaining source-integration region has a size of 768 by 1024 pixels, or $13'3 \times 17'8$ for all the cases, which is wide enough to collect all the photons from the Crab Nebula.

After subtracting the background, taking into account the sizes of the regions, we fitted the spectra taken with the four XIS modules with a model composed of a power law with photoelectric absorption using XSPEC (Arnaud 1996) version 11.2. For the photoelectric absorption, we have adopted the model `phabs` with the solar metal composition (Anders & Grevesse 1989). We first set all parameters free, allowing them to vary independently for all the XIS modules. The results are summarized for the XIS/HXD-default positions separately in table 3, and are shown in Fig. 10. In doing the fit, we adopted `ae_xi[0123]_20060213.rmf` as the RMF, and `ae_xi[0123]_xisnom6_20060615.arf` or `ae_xi[0123]_hxdnom6_20060615.arf` as the ARF for the XIS and HXD-default positions, respectively. These ARFs are made for use for a point source, whereas the Crab Nebula is slightly extended ($\sim 2'$). We thus created ARFs by utilizing the ray-tracing simulator (Misaki et al. 2005) with a Chandra image as the input, and have confirmed that the difference of the effective area between these two sets of ARFs is less than 1%. We have neglected the energy channels below 1 keV, above 10 keV, and in the 1.5–2.0 keV band because of insufficient calibration related to uncertainties of the nature and the amount of the contaminant on the OBF and Si edge structure (Koyama et al. 2006). Those energy channels are retrieved after the fit and shown in Fig. 10.

Table 3. Best-fit parameters of the power law model to the Crab spectra taken in 2005 September 15-16.

Sensor ID	N_{H}^{a}	Photon Index	Normalization ^b	Flux ^c	χ^2_{ν} (d.o.f.)
XIS-default position					
XIS0	0.35 ± 0.01	2.13 ± 0.02	$10.48^{+0.27}_{-0.26}$	2.15	0.97 (199)
XIS1	0.30 ± 0.01	2.07 ± 0.02	9.52 ± 0.23	2.14	1.27 (217)
XIS2	0.33 ± 0.01	2.09 ± 0.02	$10.09^{+0.26}_{-0.25}$	2.19	1.05 (200)
XIS3	0.34 ± 0.02	2.07 ± 0.02	$9.46^{+0.25}_{-0.24}$	2.13	1.11 (197)
HXD-default position					
XIS0	0.35 ± 0.02	2.14 ± 0.02	$9.79^{+0.31}_{-0.30}$	1.97	1.21 (155)
XIS1	0.29 ± 0.02	2.09 ± 0.02	$8.90^{+0.27}_{-0.26}$	1.94	1.07 (170)
XIS2	0.33 ± 0.02	2.10 ± 0.02	$9.89^{+0.28}_{-0.27}$	2.13	1.03 (181)
XIS3	0.32 ± 0.02	2.06 ± 0.02	$9.38^{+0.27}_{-0.26}$	2.15	1.19 (180)

^a Hydrogen column density in a unit of 10^{22}cm^{-2} .^b Power-law normalization in a unit of photons $\text{cm}^{-2} \text{s}^{-1} \text{keV}^{-1}$ at 1 keV.^c Energy flux in a unit of $10^{-8} \text{cm}^{-2} \text{s}^{-1}$ in the 2-10 keV band.

Toor & Seward (1974) compiled the results from a number of rocket and balloon measurements available at that time, and derived the photon index and the normalization of the power law of the Crab nebula to be 2.10 ± 0.03 and $9.7 \text{ photons cm}^{-2} \text{s}^{-1} \text{keV}^{-1}$ at 1 keV, respectively. Overlaying photoelectric absorption with $N_{\text{H}} = 3 \times 10^{21} \text{ cm}^{-2}$, we obtain the flux to be $2.09 \times 10^{-8} \text{ erg cm}^{-2} \text{s}^{-1}$ in the 2–10 keV band. The best-fit parameters of all the XIS modules at the XIS-default position are close to these standard values. Although those at the HXD-default position show similar values, the fluxes of XIS0 and XIS1 are smaller than the standard value by 6–7 %. Since the optical axes of these two detectors are farther away from the HXD-default position than those of the other two (Fig. 8), this may be due to insufficient calibration of the optical axes and/or the vignetting (§3.3).

Since the best-fit parameters of the four XIS modules are close to the standard values, we have attempted to constrain the hydrogen column density and the photon index to be common among all the detectors. The best-fit parameters are summarized in table 4. The hydrogen column density $(0.32\text{--}0.33) \times 10^{22} \text{cm}^{-2}$ and the photon index 2.09 ± 0.01 are consistent with the standard values.

Finally we would like to remark on our choice of the background-integration region. Since the background-integration region is taken at the very edge of the XIS field of view, one may suspect possible under-subtraction of the background due to vignetting effects (§3.3) on the background spectra. We thus have analyzed the data of MBM12 (Lynds 1457) off-cloud observation carried out from 2006 February 6 through 8 (Smith et al. 2006). The original purpose of this observation was to collect reliable background data for the main MBM12 observation. The pointing direction $(l, b) \simeq (157^\circ 3, -36^\circ 8)$ is close to anti-galactic center like the

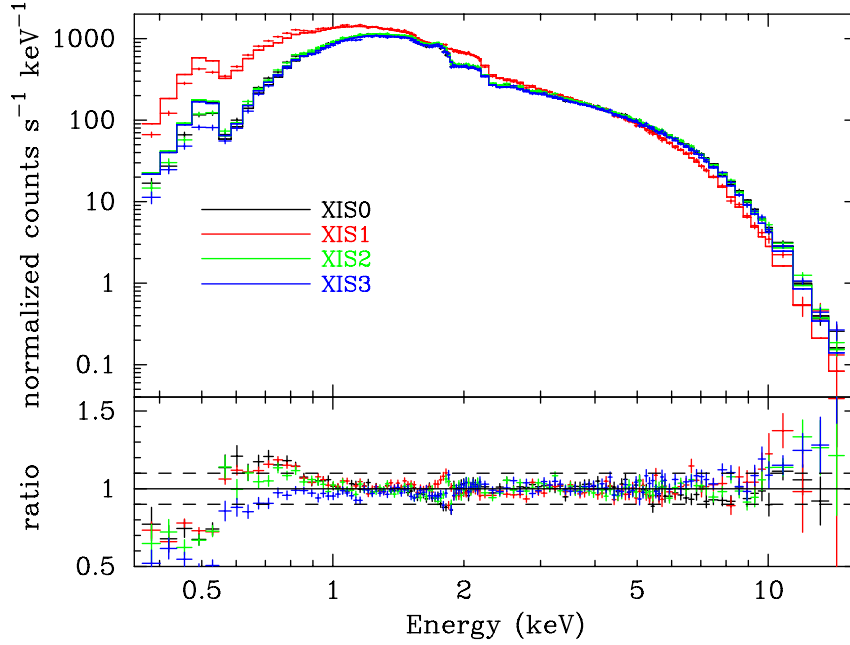


Fig. 10. Power-law fit to the Crab spectra of all the four XIS modules taken at the XIS-default position. All parameters are set free, allowing them to vary independently for each XIS module. The fit is carried out in the 1.0-10.0 keV band but excluding the interval 1.5-2.0 keV where a large systematic error associated with the Si K-edge remains, and the other channels are retrieved after the fit.

Crab Nebula, and hence, this field is a good background sky also for Crab. In the MBM12 off-cloud observation, the 2–10 keV flux within the same source-integration region as applied to Crab was found to be 0.06–0.07 c s⁻¹ for XIS0, 2, and 3 (FI) and 0.15 c s⁻¹ for XIS1 (BI). This is only about one part per 10⁴ of the counting rate of the Crab nebula in the same energy band. Moreover, the flux in the background-integration region was consistent with that from the source-integration region after appropriate area correction. This implies that the off-axis angle of the background-integration region is so small compared with the vignetting curve that non-X-ray background dominates over the reduction of CXB due to vignetting effects (§3.3) in the background-integration region. Consequently, we do not have to care about the under-subtraction of the background due to vignetting effects. Note also that the out-of-time events are the dominant source of the background in the observations of the Crab nebula. They are, however, not subject to vignetting, either.

3.3. Vignetting

The vignetting curves calculated by the ray-tracing simulator are compared with the observed intensities of the Crab nebula at various off-axis angles in Fig. 11. We have utilized the data of the Crab Nebula taken during 2005 August 22–27 (§3.1) to search for the optical axis of each XRT. In the figure, we have drawn the vignetting curves in the two energy bands 3–6 keV and 8–10 keV. To obtain this, we first assume the spectral parameters of the Crab Nebula

Table 4. Best-fit parameters of the contemporaneous power-law fit to the Crab spectra taken in 2005 September 15-16.

Sensor ID	N_{H}^{a}	Photon Index	Normalization ^b	Flux ^c	χ^2_{ν} (d.o.f.)
XIS-default position					
XIS0	0.33 ± 0.01	2.09 ± 0.01	9.93 ± 0.13	2.17	1.22 (817)
XIS1	— ^d	— ^d	9.89 ± 0.13	2.16	
XIS2	— ^d	— ^d	10.04 ± 0.13	2.19	
XIS3	— ^d	— ^d	9.52 ± 0.13	2.08	
average			9.845	2.15	
HXD-default position					
XIS0	0.32 ± 0.01	2.09 ± 0.01	$9.22^{+0.15}_{-0.14}$	2.00	1.27 (692)
XIS1	— ^d	— ^d	9.09 ± 0.14	1.98	
XIS2	— ^d	— ^d	9.77 ± 0.15	2.13	
XIS3	— ^d	— ^d	9.65 ± 0.15	2.10	
average			9.433	2.05	

^a Hydrogen column density in a unit of 10^{22}cm^{-2} .

^b Power-law normalization in a unit of photons $\text{cm}^{-2} \text{s}^{-1} \text{keV}^{-1}$ at 1 keV.

^c Energy flux in a unit of $10^{-8} \text{cm}^{-2} \text{s}^{-1}$ in the 2–10 keV band.

^d Constrained to be the same as the corresponding parameter of XIS0.

to be a power law with $N_{\text{H}} = 0.33 \times 10^{22} \text{cm}^{-2}$, photon index = 2.09, and the normalization = $9.845 \text{ photons cm}^{-2} \text{s}^{-1} \text{keV}^{-1}$ at 1 keV. These values are the averages of the four detectors at the XIS-default position (table 4). We then calculate the counting rate of the Crab Nebula on the entire CCD field of view in every $0'.5$ step both in the Det-X and Det-Y directions using the ray-tracing simulator. Note that the abrupt drop of the model curves at $\sim 8'$ is due to the source approaching the detector edge. On the other hand, the data points provide the real counting rates in the corresponding energy bands within an aperture of $13'.3$ by $17'.8$. They consist of the observations at the five different off-axis angles $0'$, $\pm 3'.5$, and $\pm 7'.0$ both in Det-X and Det-Y directions, where the origin is the XIS-default position (§3.1). Note that the aperture adopted for the observed data can collect more than 99% of the photons from the Crab Nebula, and hence the difference of the integration regions between the simulation and the observation does not matter. Finally, we renormalize both the simulation curve and the data so that the counting rate of the simulation curve at the origin becomes equal to unity. These figures roughly show that the effective area is calibrated to within $\sim 10\%$ over the XIS field of view. We expect most of these deviations can be attributed to scattering of the optical axis orientations of the four quadrants within a telescope.

3.4. Angular Resolution

Verification of the imaging capability of the XRTs has been made with the data of SS Cyg in quiescence taken during 2005 November 2 01:02UT–23:39UT. The total exposure time was

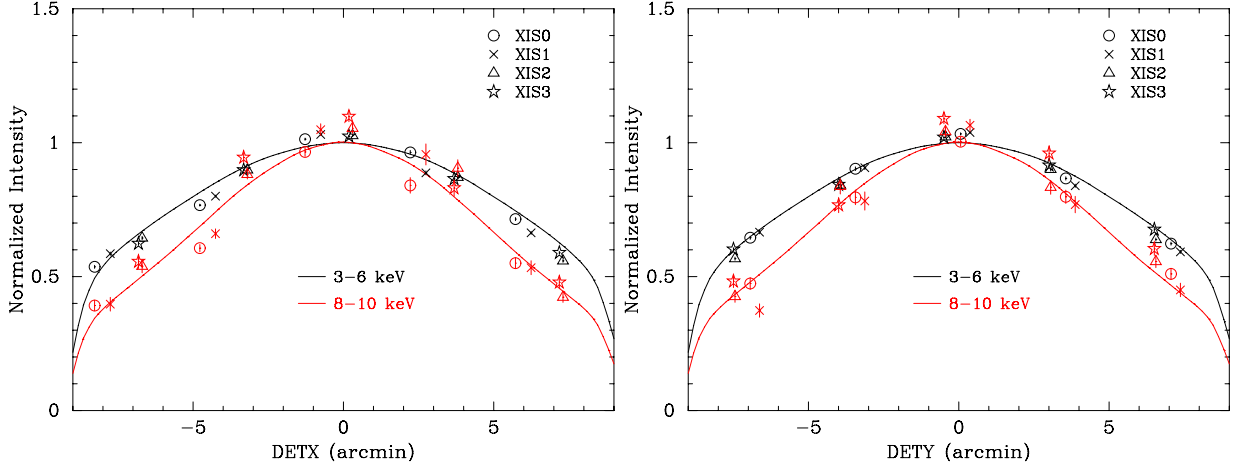


Fig. 11. Vignetting of the four XRT-I modules using the data of the Crab Nebula taken during 2005 August 22–27 in the two energy bands 3–6 keV and 8–10 keV. The model curves are calculated with the ray-tracing simulator with the spectral parameters of $N_{\text{H}} = 0.33 \times 10^{22} \text{ cm}^{-2}$, photon index = 2.09, and the normalization = $9.845 \text{ photons cm}^{-2} \text{ s}^{-1} \text{ keV}^{-1}$ at 1 keV. Note that the abrupt drop of the model curves at $\sim 8'$ is due to the source approaching the detector edge. See the text for more details. The excess of the data points of XIS1 is probably due to insufficient calibration of the backside-illuminated CCD.

41.3 ks. SS Cyg is selected for this purpose because it is a point source and moderately bright ($3.6, 5.9, 3.7$, and 3.5 c s^{-1} for XIS0 through XIS3), and hence, it is needless to care about pile-up even at the image core.

In evaluating the imaging capability, it is found that variation of the relative alignment between the XRT system and the Attitude and Orbit Controlling System (AOCS) becomes a significant problem. The variation is synchronized with the orbital motion of the spacecraft. This phenomenon is now understood to be due to the thermal distortion by the bright-earth illumination of the side panel #7 on which the instruments to measure the attitude of the spacecraft (the star trackers and the gyros) are mounted. The amplitude of the variation is as large as $\sim 50''$ at most, which cannot be neglected in evaluating the imaging capability. Software to correct this alignment variation has been developed. In the meantime, we simply accumulate the data taken while the pointing of the XRT is stable. In Fig. 12, we give the image, the Point-Spread Function (PSF), and the EEf of all the XRT-I modules thus obtained. Due to this treatment, however, the total exposure time is reduced to be 9.1 ks. The HPD is obtained to be $1/8, 2/3, 2/0$, and $2/0$ for XRT-I0, 1, 2, and 3, respectively. These values are in general consistent with those expected from ground-based calibration measurements.

3.5. Stray Light

Observations of stray light were carried out with the Crab Nebula during 2005 August 22 – September 16 (§ 3.1) at the off-axis angles of $(\text{Det-X}, \text{Det-Y}) = (\pm 20', 0'), (0', \pm 20'), (\pm 50', 0'),$ and $(0', \pm 50')$. An example stray-light image is shown in the right panel of Fig. 13. This image

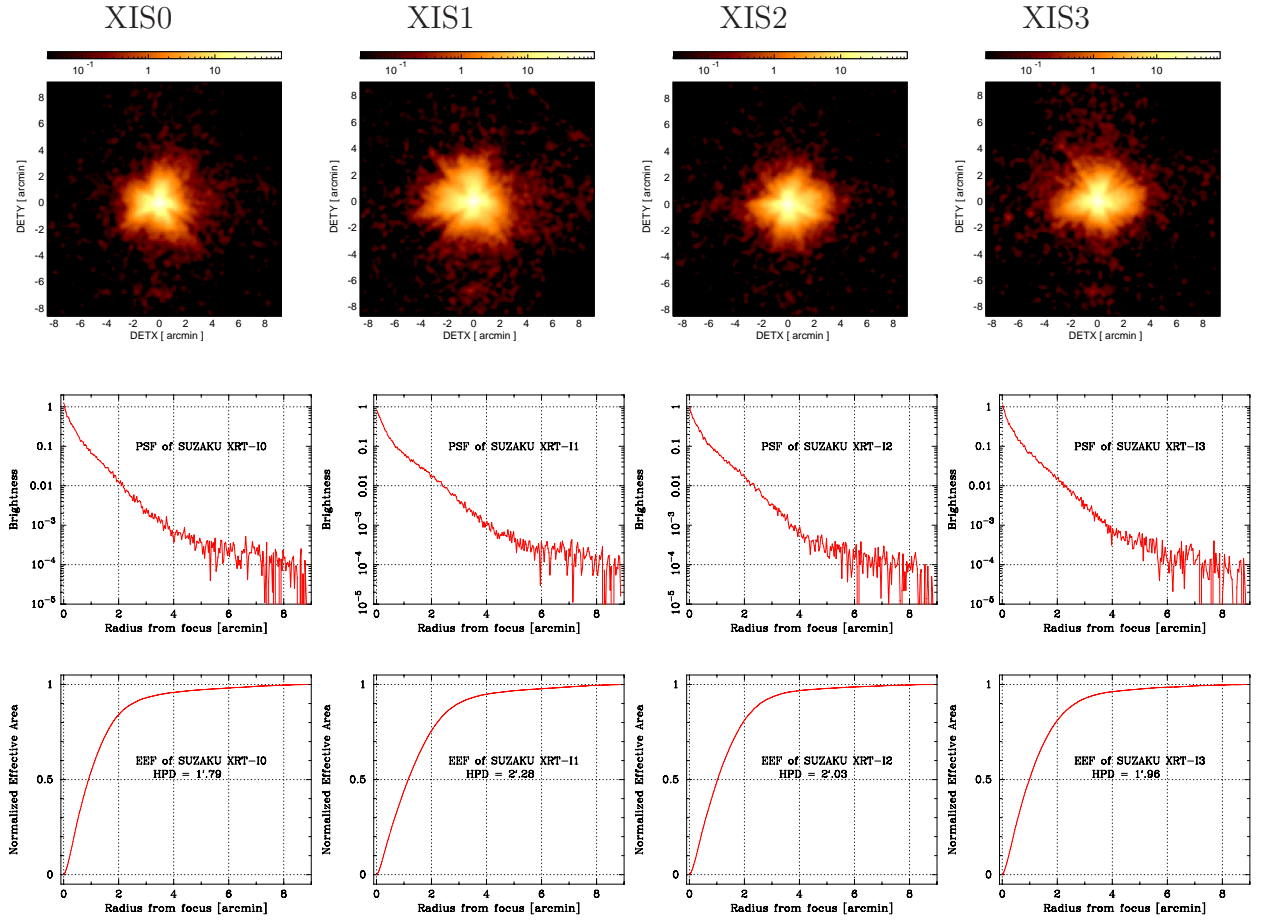


Fig. 12. Image, Point-Spread Function (PSF), and EEF of the four XRT-I modules in the focal plane. All the images are binned with 2×2 pixels followed by being smoothed with a Gaussian with a sigma of 3 pixels, where the pixel size is $24 \mu\text{m}$. The EEF is normalized to unity at the edge of the CCD chip (a square of 17.8 on a side). With this normalization, the HPD of the XRT-I0 through I3 is 1.8 , 2.3 , 2.0 , and 2.0 , respectively.

was taken with XIS3 in the $2.5\text{--}5.5$ keV band when the Crab Nebula is offset at $(\text{Det-X}, \text{Det-Y}) = (-20', 0')$. The left and central panels show simulated stray light images without and with the pre-collimator, respectively, of a monochromatic point source of 4.5 keV being located at the same off-axis angle. The ghost image seen in the left half of the field of view is due to the “secondary reflection”. Although the “secondary reflection” cannot be completely diminished at the off-axis angle of $20'$ (§ 2.3), the center of the field of view is nearly free from stray light. The semi-circular bright region in the middle panel, starting from $(\text{Det-X}, \text{Det-Y}) = (-8.9, +6.5)$ through $\sim(0', 0')$ where the image becomes fainter, and ending up at $(-8.9, -6.5)$, originates from the innermost secondary reflector, because the space between the innermost reflector and the inner wall of the telescope housing is much larger than the reflector-reflector separation. This semi-circular bright region is marginally visible in the real Crab Nebula image in the right panel. Another remarkable difference between the simulation and the real observation is the location of the brightest area; in the simulation, the left end of the image

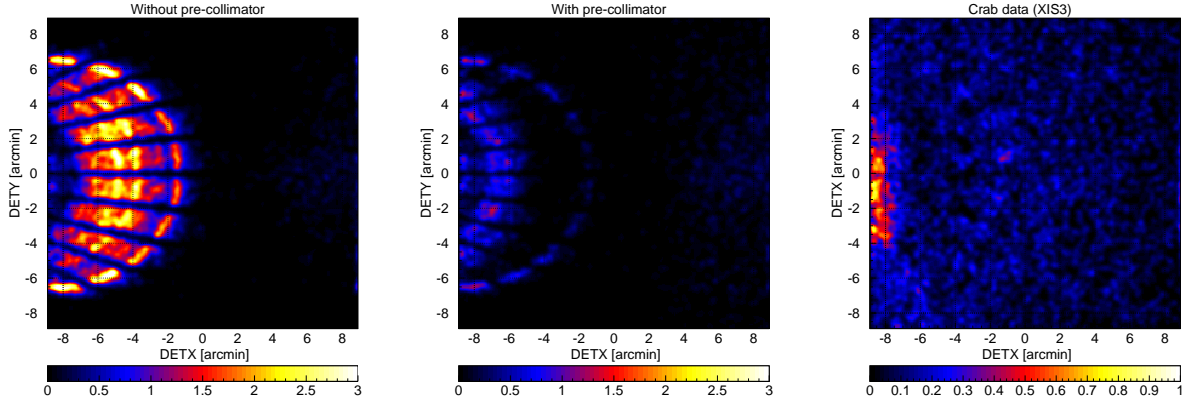


Fig. 13. Focal plane images formed by stray light. The left and middle panels show simulated images of a monochromatic point-like source of 4.51 keV locating at $(\text{Det-X}, \text{Det-Y}) = (-20', 0')$ in the cases of without and with the pre-collimator, respectively. The radial dark lanes are the shades of the alignment bars. The right panel is the in-flight stray image of the Crab Nebula in the 2.5–5.5 keV band located at the same off-axis angle. The unit of the color scale of this panel is counts per 16 pixels over the entire exposure time of 8428.8 s. The counting rate from the whole image is $0.78 \pm 0.01 \text{ c s}^{-1}$ including background. Note that the intensity of the Crab Nebula measured with XIS3 at the XIS-default position is $458 \pm 3 \text{ c s}^{-1}$ in the same 2.5–5.5 keV band. All the images are binned with 4×4 pixels followed by being smoothed with a Gaussian with a sigma of 2 pixels, where the pixel size is $24 \mu\text{m}$.

$(\text{Det-X} \lesssim -7'5, |\text{Det-Y}| \lesssim 3')$ is relatively dark whereas the corresponding part is brightest in the observed image. These differences originate from relative alignments among the primary and secondary reflectors, and the blades of the pre-collimator, which are to be calibrated by referring to the data of the stray light observations in the near future.

We have investigated systematic error of the simulated stray-light intensity by changing the relative alignments of the reflectors and the pre-collimator blades in the ray-tracing program within physically allowed ranges to find that the observed stray light intensity from the entire field of view never exceeds \sim twice of the simulated one for an off-axis angle of $20'$. If the off-axis angle is larger, the stray light intensity becomes weaker in general.

4. Conclusion

We have described the design parameters, production process, and in-flight performance of the XRTs onboard Suzaku (Mitsuda et al. 2006). The replication method adopted for reflector production for the first time reduces the mid-frequency figure error of the reflector substrate that dominates the image blur of the ASCA XRTs. Consequently, the imaging capability is significantly improved over ASCA with an HPD from $3'6$ to $1'9$. In-flight calibration has been carried out for the four XRT-I modules which focus their images on the XIS detectors (Koyama et al. 2006). The optical axes have been searched for in the focal plane with the Crab Nebula observed at the XIS-default position, $\pm 3'5$ -off, and $\pm 7'0$ -off positions both in the Det-X and Det-Y directions. As a result, they are found to concentrate within $r < 1'3$ from

the XIS-default position. This makes the observation efficiency of all the XRTs more than 97% even at the high-energy limit 8–10 keV. The optical axis of the HXD PIN, however, is away from the XIS-default position by $\sim 5'$ in the negative Det-X direction. We thus have provided another default pointing position, the HXD-default position, for HXD-oriented observations, which is (Det-X, Det-Y) = $(-3.5, 0')$. Vignetting calibration within the XIS field of view has been carried out with the same Crab data. The observed vignetting is consistent with that calculated according to the telescope design and the spectral parameters summarized by Toor & Seward (1974) within $\sim 10\%$. From a contemporaneous fit of a power law to all the XIS spectra taken at the XIS/HXD-default positions, we have found the hydrogen column density and the photon index to be $(0.32-0.33) \times 10^{22} \text{cm}^{-2}$ and 2.09 ± 0.01 , respectively. The fluxes obtained from these fits are consistent with that predicted by Toor & Seward (1974) within $\sim 3\%$. The in-flight imaging capability is what we have expected from ground-based calibration. Using the data of SS Cyg in quiescence, we have found that HPDs are in the range 1'8–2'3. In order to reduce stray light photons, which arrive at the XIS detector from directions out of the field of view, each XRT module is equipped with a pre-collimator. The pre-collimator works as expected, and it successfully reduces the stray lights from the directions of 20' and 50'-off from the XIS-default position.

Acknowledgement

The authors are grateful for dedicated contribution to the XRT production, pre-launch calibration and various tests provided by the following people: Y. Terashima, M. Watanabe, K. Haga, T. Yoshioka, H. Takada, K. Matsunaga, S. Fukuda, T. Tanaka from Nagoya University: M. Itoh, S. Akao, K. Imamura from Kobe University: H. Honda, K. Okada, T. Endo, J. Ishida, Y. Hidaka, M. Maeda from ISAS/JAXA: T. Shimizu from Tokyo Metropolitan University: Curtis O'dell and technical staff and contractors at NASA/GSFC. The machine shop of Nagoya University kindly supported us from technical aspect. The authors are grateful to B. Budau, W. Burkert, M. J. Freyberg, G. Hartner, G. Hasinger who kindly provided an opportunity to calibrate XRT-I0 at the Panter test facility in Germany. The authors would like to express our special thanks to Koichi Yamashiro, Hideo Yanai, Yusuke Hataide, Kazuhiro Abe, Hitoshi Kaneko, Takashi Sasaki, and Osamu Kubota from NIPPI Corporation for designing, constructing, and testing the Extensible Optical Bench. The synchrotron radiation experiments were performed at the BL25SU beamline in the SPring-8 with the approval of the Japan Synchrotron Radiation Research Institute (JASRI) (Proposal No. 2006A1221). This research was supported in part by a grand in aid of Specially Promoted Research contract (15001002) from the Ministry of Education, Culture, Sports, Science and Technology.

References

- Anders, E., & Grevesse, N. 1989, *Geochim. Cosmochim. Acta*, 53, 197
- Arnaud, K. A. 1996, *ASP Conf. Ser. 101: Astronomical Data Analysis Software and Systems V*, 101, 17
- Aschenbach, B. 2002, *Proc. SPIE*, 4496, 8
- Aschenbach, B. 1988, *Appl. Opt.*, 27, 1404
- Burke, B. E., Mountain, R. W., Harrison, D. C., Bautz, M. W., Doty, J. P., Ricker, G. R., & Daniels, P. J. 1991, *IEEE Trans. ED-38*, 1069
- Burrows, D. N., et al. 2005, *Space Science Reviews*, 120, 165
- Conti, G., Mattaini, E., Santambrogio, E., Sacco, B., Cusumano, G., Citterio, O., Braeuninger, H. W., & Burkert, W. 1994, *Proc. SPIE*, 2279, 101
- de Korte, P. A. J., Giralt, R., Coste, J. N., Ernu, C., Frindel, S., Flamand, J., & Contet, J. J. 1981, *Appl. Opt.*, 20, 1080
- Inoue, H. 2003, *Advances in Space Research*, 32, 2089
- Ishisaki, Y. et al. 2006, *PASJ*, this volume
- Koyama, K. et al. 2006, *PASJ*, this volume
- Kelley, R. et al. 2006, *PASJ*, this volume
- Kokubun, M. et al. 2006, *PASJ*, this volume
- Kunieda, H., et al. 2001, *Appl. Opt.*, 40, 553
- Lumb, D. H., Finoguenov, A., Saxton, R., Aschenbach, B., Gondoin, P., Kirsch, M., & Stewart, I. M. 2003, *Proc. SPIE*, 4851, 255
- Misaki, K., et al. 2005, *Appl. Opt.*, 44, 916
- Mitsuda, K. et al. 2006, *PASJ*, this volume
- Mori, H., et al. 2005, *PASJ*, 57, 245
- Serlemitsos, P. J., & Soong, Y. 1996, *Ap&SS*, 239, 177
- Serlemitsos, P. J., et al. 1995, *PASJ*, 47, 105
- Serlemitsos, P. J. 1988, *Appl. Opt.*, 27, 1447
- Shibata, R., et al. 2001, *Appl. Opt.*, 40, 3762
- Smith, R. K. et al. 2006, *PASJ*, this volume
- Takahashi, T. et al. 2006, *PASJ*, this volume
- Tanaka, Y., Inoue, H., & Holt, S. S. 1994, *PASJ*, 46, 37L
- Toor, A., & Seward, F. D. 1974, *AJ*, 79, 995
- Van Speybroeck, L. 1979, *Proc. SPIE*, 184, 2
- Weisskopf, M. C., Brinkman, B., Canizares, C., Garmire, G., Murray, S., & Van Speybroeck, L. P. 2002, *PASP*, 114, 1
- Zissa, D. E., 1999, *Proc. SPIE*, 3766, 36